

## RESEARCH ARTICLE

10.1002/2016GB005418

## Key Points:

- Iron concentrations are partitioned according to source and time since injection into the ocean for a family of inverse-model estimates
- Iron concentration anomalies due to source removal underestimate the true source contribution because scavenging is nonlinear
- Most iron in the Southern Ocean euphotic zone is upwelled regenerated iron deposited from the atmosphere several hundred years earlier

## Correspondence to:

M. Holzer,  
mholzer@unsw.edu.au

## Citation:

Holzer, M., M. Frants, and B. Pasquier (2016), The age of iron and iron source attribution in the ocean, *Global Biogeochem. Cycles*, 30, 1454–1474, doi:10.1002/2016GB005418.

Received 27 MAR 2016

Accepted 12 SEP 2016

Accepted article online 20 SEP 2016

Published online 12 OCT 2016

Corrected 18 OCT 2016

This article was corrected on 18 OCT 2016. See the end of the full text for details.

## The age of iron and iron source attribution in the ocean

Mark Holzer<sup>1,2</sup>, Marina Frants<sup>3</sup>, and Benoît Pasquier<sup>1</sup>

<sup>1</sup>Department of Applied Mathematics, School of Mathematics and Statistics, University of New South Wales, Sydney, NSW, Australia, <sup>2</sup>Also at Department of Applied Physics and Applied Mathematics, Columbia University, New York, New York, USA, <sup>3</sup>Department of Oceanography, Graduate School of Engineering and Applied Sciences, Naval Postgraduate School, Monterey, CA

**Abstract** We use tracers to partition dissolved iron (dFe) into the contributions from each source within a numerical model of the iron cycle without perturbing the system. These contributions are further partitioned according to the time since injection into the ocean, which defines their iron-age spectrum and mean iron age. The utility of these diagnostics is illustrated for a family of inverse model estimates of the iron cycle, constrained by a data-assimilated circulation and available dFe measurements. The source contributions are compared with source anomalies defined as the differences between solutions with and without the source in question. We find that in the Southern Ocean euphotic zone, the hydrothermal and sediment contributions range from 15% to 30% of the total each, which the anomalies underestimate by a factor of  $\sim 2$  because of the nonlinearity of scavenging. The iron age is only reset by scavenging and attains a mean of several hundred years in the Southern Ocean euphotic zone, revealing that aeolian iron there is supplied primarily from depth as regenerated dFe. Tagging iron according to source region and pathways shows that 70–80% of the aeolian dFe in the euphotic zone near Antarctica is supplied from north of 46°S via paths that reach below 1 km depth. Hydrothermal iron has the oldest surface mean ages on the order of middepth ventilation times. A measure of uncertainty is provided by the systematic variations of our diagnostics across the family of iron cycle estimates, each member of which has a different aeolian source strength.

## 1. Introduction

Iron is a limiting micronutrient in much of the world oceans, and a lack of dissolved iron (dFe) has been shown to account for the ocean's high-nutrient low-chlorophyll regions [Martin *et al.*, 1990; de Baar *et al.*, 1995; Landry *et al.*, 1997; Boyd *et al.*, 2007]. The transport pathways and timescales of iron in the ocean are key for understanding how the marine iron cycle operates, but they are just beginning to be studied [e.g., Tagliabue *et al.*, 2014]. Important open questions about iron transport remain, such as the following: What is the relative importance of old regenerated iron upwelling from depth versus freshly dissolved iron deposited from the atmosphere in determining the euphotic-zone dFe concentration? Here we build on the iron inverse modeling of Frants *et al.* [2016] to compute (i) the contributions from the individual iron sources to the total dFe concentration and (ii) the mean time since iron was injected by these sources, which we will refer to as the mean iron age.

A highly uncertain aspect of the marine iron cycle is the strengths of the aeolian, sedimentary, and hydrothermal iron sources and the contribution that each source makes to the total dissolved iron concentration [e.g., Moore and Braucher, 2008; Tagliabue *et al.*, 2016]. The contribution from hydrothermal vents to bioavailable iron in the euphotic zone is typically estimated to have a  $\sim 0.02$ – $0.05$  nM concentration [Tagliabue *et al.*, 2010; Frants *et al.*, 2016] or roughly 10% of the total. In a model context, these source attributions are typically made by computing the dFe fields with and without a hydrothermal source and calculating the difference usually referred to as the “anomaly” due to the source [e.g., Tagliabue *et al.*, 2010]. While the anomalies answer the question of how the iron cycle would be different if the source in question were absent, the anomalies do not quantify the contribution that the source makes to the dFe field in the state of the system with the source present. This is because of the nonlinear nature of iron scavenging: the iron cycle operates differently when the sources are present compared to when they are absent. Here we calculate the true source contributions in the unperturbed system and show that the source anomalies can underestimate them by as much as a factor of 2.

By partitioning the iron from a given source according to the time since injection into the ocean (i.e., according to age), we compute the iron-age spectra and mean iron ages for each source at every point in the ocean. In the euphotic zone, we find that the iron age due to all sources is oldest in the Southern Ocean, exceeding several hundred years near Antarctica. The mean iron age is dominated by the aeolian iron component because hydrothermal and sedimentary iron, while being on average older still, have generally lower concentrations. Our analysis shows that the majority of dFe in the Southern Ocean euphotic zone is upwelled from a deep old regenerated reservoir and that the upwelling iron was deposited from the atmosphere at lower latitudes as much as centuries before becoming available in the Southern Ocean.

## 2. The Model

### 2.1. Iron Model

We use the simple data-constrained iron cycling model of *Frants et al.* [2016] embedded in the steady data-assimilated global circulation of *Primeau et al.* [2013]. The circulation has a horizontal resolution of  $2^\circ \times 2^\circ$  and 24 vertical levels, ranging in thickness from 36 m at the surface to  $\sim 600$  m in the deepest ocean. The iron model is formulated in terms of the total dFe concentration, which is the sum of the ligand-chelated iron and free iron concentrations. Ligand concentrations are prescribed to be enhanced above an otherwise uniform background of 1 nM in (i) hydrothermal plumes where the grid box averaged concentrations of finite-lifetime ligands were clamped at 3 nM at the vent injection sites and allowed to spread from there with the flow and in (ii) old waters where ligand concentrations were elevated by a factor of roughly 2. Enhancement in hydrothermal plumes was based on the observations of *Bennett et al.* [2008] and *Hawkes et al.* [2013] and on the modeling by *Sander and Koschinsky* [2011], while the enhancement in old waters was supported by the modeling of *Misumi et al.* [2013]. Free and total iron are related through quadratically nonlinear chemical equilibrium. Iron is injected into the ocean by an aeolian source  $S_A$ , a sedimentary source  $S_S$ , and a hydrothermal source  $S_H$ . For  $S_A$ , we adopt the geographic pattern of the soluble iron flux from the atmospheric modeling of *Luo et al.* [2008], which includes detailed modeling of atmospheric processing and solubility. We assume that the large scales of this pattern are reasonably robust but treat the overall amplitude as an uncertain adjustable model parameter that is varied for a family of solutions (see below). The sedimentary source is keyed to the organic matter flux onto the ocean bottom following *Elrod et al.* [2004], and the pattern of the hydrothermal sources is taken from the  $^3\text{He}$  source of the OCMIP protocol [*Dutay et al.*, 2004], with different optimized amplitudes for each basin. (The ranges of the ratio of the optimized hydrothermal iron source to the mantle  $^3\text{He}$  source across the family of inverse model estimates were  $(1.4 - 1.6) \times 10^6$ ,  $(3.8 - 5.8) \times 10^5$ , and  $(3.2 - 6.9) \times 10^5$  in units of  $(\text{mol Fe yr}^{-1})/(\text{mol } ^3\text{He yr}^{-1})$ , for the Atlantic, Pacific, and Indian Ocean basins, respectively.) Because the aeolian source pattern is important in our analysis below, the zonally integrated  $S_A$  is plotted in Appendix A.

The steady state total dFe concentration  $\chi$  obeys

$$\mathcal{T}\chi = S_A + S_S + S_H - R(\chi)J_{\text{PO}_4} + SR(\chi)J_{\text{PO}_4} - J_{\text{sc}}(\chi), \quad (1)$$

where  $\mathcal{T}$  is the advective-eddy-diffusive transport operator and  $S$  is an operator that assigns a fraction  $\sigma$  of the phosphate uptake  $J_{\text{PO}_4}$  to remineralization at depth with a Martin curve (i.e.,  $S$  is the particle sinking and remineralization operator). The phosphate uptake rate per unit volume,  $J_{\text{PO}_4}$ , was parameterized in terms of satellite estimates of net primary production,  $J_{\text{NPP}}$ , as  $J_{\text{PO}_4} = \alpha J_{\text{NPP}}^\eta$ , with the coefficients  $\alpha$  and  $\eta$  optimized to minimize the volume-weighted quadratic misfit in the  $\text{PO}_4$  concentration between a separate phosphorus cycling model and the observational climatology as described by *Frants et al.* [2016]. This parameterization of  $J_{\text{PO}_4}$  was inspired by the work of *Hansell et al.* [2012] and *Teng et al.* [2014] and produces an export production with a realistic pattern. Our optimal values for  $\alpha$  and  $\eta$  lie within the Bayesian error bounds independently determined by *Teng et al.* [2014]. Iron uptake per unit volume,  $RJ_{\text{PO}_4}$ , is related to phosphate uptake by the Fe:P stoichiometric ratio,  $R$ , modeled as depending on the iron concentration through a Michaelis-Menten factor following *Galbraith et al.* [2010]. As organic phosphorus remineralizes, the term  $SRJ_{\text{PO}_4}$  releases dFe at depth with the same Fe:P stoichiometric ratio. The term  $J_{\text{sc}}$  in (1) is the iron scavenging rate per unit volume. Scavenging is assumed to have the same geographic pattern as organic matter production and a vertical profile that decreases with depth according to a power law. The profile is assumed not to fall below an optimized minimum value to capture scavenging by ballast particles. This minimum scavenging may also effectively capture scavenging by dust—for this model, we found no benefit in explicitly adding dust or additional inorganic scavenging. The scavenging acts only on free iron and is hence a quadratically nonlinear function of

$\chi$  by virtue of the chemical equilibrium between free dFe, chelated dFe, and ligands. Scavenged iron is not tracked in a particulate iron pool—once iron has been scavenged, it is assumed to be lost forever. Relaxing this assumption by explicitly incorporating transport and redissolution of scavenged iron and reoptimizing parameters turns out not to alter our results qualitatively—see section 4. Colloidal iron is neglected.

The scavenging and source parameters of the iron model were sequentially optimized by minimizing the quadratic mismatch between modeled and available observed dFe concentrations, which were taken from the data set compiled by *Tagliabue et al.* [2012] and the GEOTRACES intermediate data product [*Mawji et al.*, 2015]. However, *Frants et al.* [2016] found that the dFe concentration data itself do not suffice to constrain the strength,  $\sigma_A$ , of the aeolian source (the global integral of  $S_A$ ) because of significant spatial overlap between effective sources and the scavenging sink. Instead, a family of solutions with  $\sigma_A$  ranging from 0.3 to 14 Gmol/yr was found to match the available dFe concentration data to nearly the same fidelity, with solutions for  $\sigma_A > 6.1$  Gmol/yr yielding unrealistic patterns of iron limitation. Once  $\sigma_A$  is specified, the other parameters are uniquely determined. As in *Frants et al.* [2016], we focus on the  $\sigma_A = 3.5$  Gmol/yr case as being representative of the entire family and then establish the systematic variations of bulk quantities across the family of solutions. For additional details on the iron inverse model, see the paper by *Frants et al.* [2016].

## 2.2. Diagnostic Linear Model

For a given solution  $\chi_{nl}$  of (1), we build an equivalent linear iron model so that the source contributions and transit-time distributions of dFe can be computed rigorously without changing the dynamical state of the iron cycle. The basic idea is that once the uptake rate of iron  $J_{up}(\chi) \equiv R(\chi) J_{PO4}$  and its loss rate  $J_{sc}(\chi)$  are known, we can determine the local rate coefficients at point  $\mathbf{r}$  with which any subset of the iron is taken up or lost:

$$\gamma_{up}(\mathbf{r}) = J_{up}(\chi_{nl}(\mathbf{r})) / \chi_{nl}(\mathbf{r}) \quad \text{and} \quad \gamma_{loss}(\mathbf{r}) = J_{sc}(\chi_{nl}(\mathbf{r})) / \chi_{nl}(\mathbf{r}) \quad . \quad (2)$$

For example, if  $\chi_{nl}$  is considered the sum of aeolian, sedimentary, and hydrothermal contributions,  $\chi_{nl} = \chi_A + \chi_S + \chi_H$ , the uptake of the aeolian subset must be given by  $\gamma_{up} \chi_A$ , that is, the uptake of a subset of the iron molecules is taken up in proportion to its concentration, and similarly for the loss due to scavenging.

## 2.3. Green Function, Source Contribution, and Mean Age

The linear diagnostic model allows us to label dFe with passive tracers to track it from source to sink as follows: First, we discretize the dFe concentration and source fields on the computational grid and organize them into column vectors  $\mathbf{x}$  and  $\mathbf{s}$ , respectively. Correspondingly, the transport operator,  $\mathcal{T}$ , and sinking plus remineralization operator,  $\mathcal{S}$ , are discretized and organized into sparse matrices  $\mathbf{T}$  and  $\mathbf{S}$ , so that the equivalent linear model can be written as

$$\mathbf{T}\mathbf{x} = (-\mathbf{U} + \mathbf{S}\mathbf{U})\mathbf{x} - \mathbf{L}\mathbf{x} + \sum_i \mathbf{s}_i \quad , \quad (3)$$

where  $\mathbf{U} = \text{diag}(\gamma_{up})$  is the diagonal (i.e., local) linear uptake operator and  $\mathbf{L} = \text{diag}(\gamma_{loss})$  is the diagonal linear scavenging operator. The index  $i$  runs over the three source types: aeolian, sedimentary, and hydrothermal. Note that, by construction, the diagnostic system (3) has the exact same solution as the nonlinear system (1).

Collecting the linear operators of (3) into matrix  $\mathbf{A} \equiv \mathbf{T} + \mathbf{U} - \mathbf{S}\mathbf{U} + \mathbf{L}$ , the contribution  $\mathbf{g}_i(t)dt$  of the iron concentration due to injection by the  $i$ th source, during time interval  $dt$  a time  $t$  ago, obeys

$$\partial_t \mathbf{g}_i(t) + \mathbf{A}\mathbf{g}_i(t) = \mathbf{s}_i \delta(t) \quad , \quad (4)$$

where  $\delta(t)$  is the Dirac delta function. The vector  $\mathbf{g}_i$  is a Green function for source  $\mathbf{s}_i$  [e.g., *Holzer and Hall*, 2000; *Holzer and Primeau*, 2013].

Denoting the time integral  $\int_0^\infty (\dots) dt$  by  $\langle \dots \rangle$ , the temporal moments of  $\mathbf{g}_i(t)$  follow from (4) as

$$\langle \mathbf{g}_i \rangle = \mathbf{A}^{-1} \mathbf{s}_i \quad , \quad (5)$$

and, for integer  $n \geq 1$ ,

$$\langle t^n \mathbf{g}_i \rangle = n \mathbf{A}^{-1} \langle t^{n-1} \mathbf{g}_i \rangle \quad . \quad (6)$$

Note that the steady state dFe concentration vector due to source  $\mathbf{s}_i$  is given by  $\mathbf{x}_i = \langle \mathbf{g}_i \rangle$ , and the dFe concentration due to all sources is given by  $\mathbf{x} = \sum_i \langle \mathbf{g}_i \rangle$ .

The mean iron age is now simply defined as the mean time since iron was injected by the source. This mean age is well defined for the population of dissolved iron molecules, with the sources providing a constant supply

of newly “born” iron molecules and the scavenging providing the balancing “death” process. Denoting the three-dimensional field associated with vector  $\mathbf{g}_i(\mathbf{r}, t)$  by  $g_i(\mathbf{r}, t)$ , the local mean age of dFe due to source  $S_i$  at point  $\mathbf{r}$  is given by

$$\Gamma_{\text{Fe}}^i(\mathbf{r}) = \frac{\langle t g_i(\mathbf{r}, t) \rangle}{\langle g_i(\mathbf{r}, t) \rangle}. \quad (7)$$

We refer to the quantity  $p_i(\mathbf{r}, t) \equiv g_i(\mathbf{r}, t) / \langle g_i(\mathbf{r}, t) \rangle$  as the iron-age spectrum at point  $\mathbf{r}$ :  $p_i(\mathbf{r}, t)$  is the normalized distribution of the time  $t$ , or age, since the iron at  $\mathbf{r}$  was last injected (born) by source  $S_i$  (aeolian, sedimentary, or hydrothermal). Similarly, we can also define the mean iron age for an entire subvolume  $V$  of the ocean (e.g., a cluster of grid boxes—see below) by

$$\Gamma_{\text{Fe}, V}^i = \frac{\int_V d^3r \langle t g_i(\mathbf{r}, t) \rangle}{\int_V d^3r \langle g_i(\mathbf{r}, t) \rangle}. \quad (8)$$

Note that the mean iron age,  $\Gamma_{\text{Fe}}(\mathbf{r})$  of the total iron at point  $\mathbf{r}$  (due to the total source) is given by the concentration weighted sum

$$\Gamma_{\text{Fe}}(\mathbf{r}) = \frac{1}{\chi(\mathbf{r})} \sum_i \chi_i(\mathbf{r}) \Gamma_{\text{Fe}}^i(\mathbf{r}). \quad (9)$$

We emphasize that the mean iron age, unlike the ideal mean age of water (the mean transit time from the surface), need not be zero at the surface. The age clock of iron starts at source injection (birth) and stops when the iron is scavenged (death), while the age clock for water is reset to zero at surface contact. The mean iron age is hence the mean source-to-scavenging time, or in a population analogy, the mean birth-to-death lifetime of dissolved iron.

### 3. Results

#### 3.1. Source Contributions

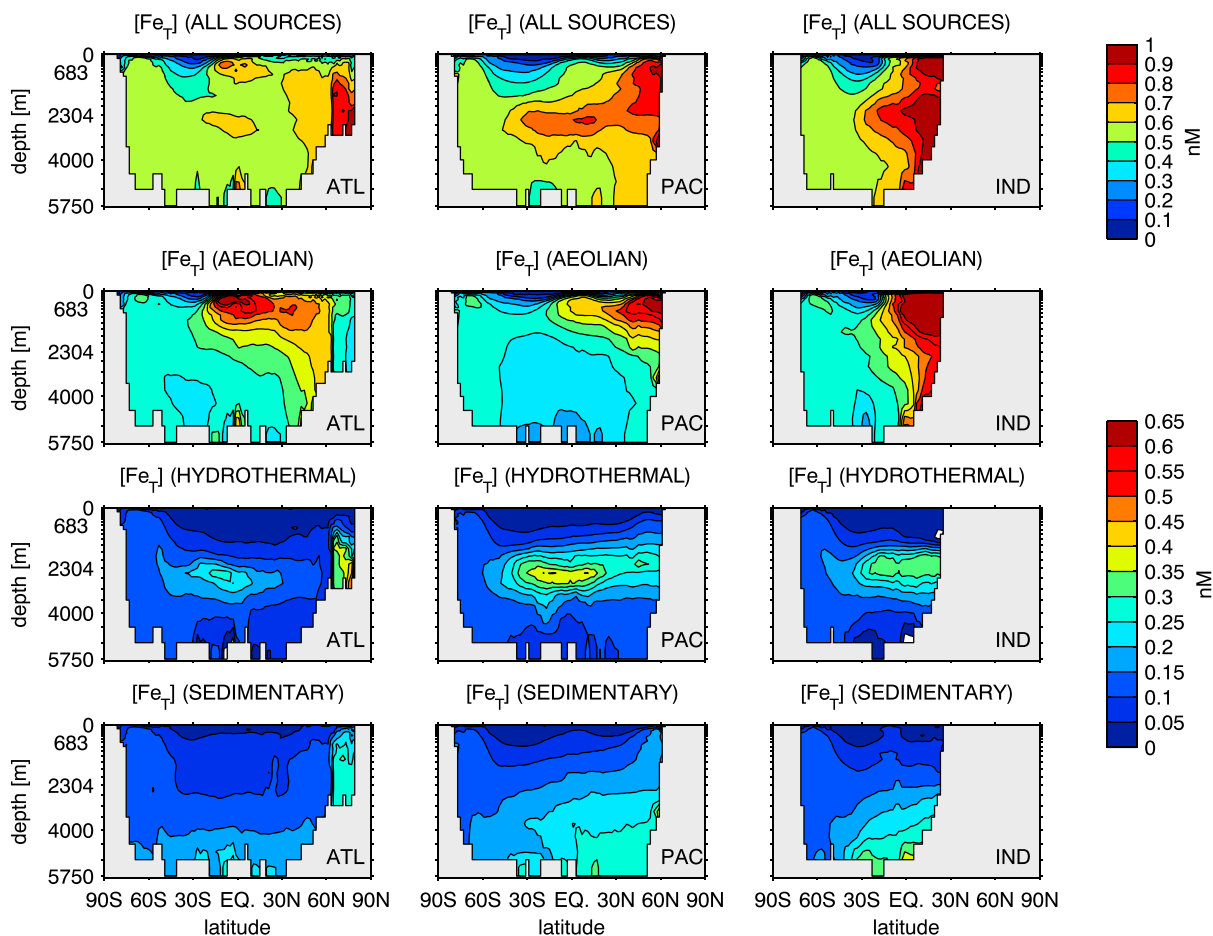
Figure 1 shows the dFe concentrations due to each of the three sources,  $\chi_i \equiv \langle g_i \rangle$ , zonally averaged for each basin for our representative case of an aeolian source strength  $\sigma_A = 3.5 \text{ Gmol/yr}$ . In the upper ocean, aeolian iron is the largest contributor to the zonally averaged total dFe concentration. In the North Atlantic, the surface influence reaches down with North Atlantic Deep Water, but the deep concentrations are attenuated by scavenging. The highest aeolian iron concentrations occur in the upper tropical Atlantic and Indian Ocean where the aeolian source (dust plus combustion deposits [Luo *et al.*, 2008]) is highest. A tongue of aeolian iron can be seen in the Southern Ocean reaching from depth to the surface with upwelling Circumpolar Deep Water. The high southern latitudes have relatively weak atmospheric iron sources (Appendix A), and we will show below that the bulk of the iron in the Southern Ocean euphotic zone is old aeolian iron that was biologically pumped to depth and then upwells as regenerated dFe.

Hydrothermal iron is found at middepths where the mid-ocean ridges vent hydrothermal fluid. The mid-Atlantic ridge surfaces at Iceland leading to a maximum in the hydrothermal dFe concentration north of  $60^\circ\text{N}$ . In the Southern Ocean, the hydrothermal sources are weak (at least in our inverse-model estimate), but a plume of diluted hydrothermal iron of  $\sim 0.1 \text{ nM}$  concentration can be seen reaching toward the Southern Ocean surface in all basins.

The sedimentary iron source is largest on the continental shelves, but these shallow sedimentary sources make only small contributions to the total iron concentrations because biological production and, hence scavenging, are also strong where the sedimentary sources are strong. Excepting the polar North Atlantic, the largest sedimentary iron contributions occur in the abyssal basins. On the abyssal planes, the sedimentary source, modeled to scale with the flux of organic matter, is weak, but so are the ventilation rates and the scavenging so that the small sources can build up substantial dFe concentrations before either attaining high enough gradients to drive eddy-diffusive dilution or being scavenged by ballast particles. This picture is supported by the mean age of sedimentary iron discussed below, which can reach several hundred years in the deep ocean. As with the aeolian and hydrothermal iron, sedimentary iron reaches toward the Southern Ocean surface with upwelling deep waters.

##### 3.1.1. Source Contributions Versus Source Anomalies

Because our numerical formulation of the steady state iron cycle allows us to easily construct an equivalent linear model, we are able to efficiently compute the exact dFe contributions from each source. For a dynamical

dFe contributions for  $\sigma_A = 3.5$  Gmol/year


**Figure 1.** Zonally averaged dFe concentrations for each basin due to all sources and the contributions from the aeolian, hydrothermal, and sedimentary sources. The three contributions sum to the total (all sources) shown in the top panels. Note the separate color scales for total dFe and contributions.

biogeochemical forward model, attributing the effect of a given source is less simple, and researchers tend to solve the system with and without the source in question and attribute the difference between solutions,  $\Delta\chi_i = \chi - \chi(\text{no } S_i)$ , i.e., the “anomaly,” to the source  $S_i$ . For example, *Frants et al.* [2016] and *Tagliabue et al.* [2010] take this approach to compute a dFe anomaly due to the hydrothermal source. For a linear system, the two approaches are equivalent, but because scavenging acts only on free iron determined from the total dFe concentration through nonlinear chemical equilibrium, the iron cycle is nonlinear and anomalies and true source contributions are generally different.

We find that the spatial patterns of the source contributions and the corresponding anomalies are qualitatively similar, but there are important quantitative differences. Figure 2 shows that the zonally averaged differences between anomalies and contributions are negative in all basins and for all sources: The anomalies underpredict the true contribution virtually everywhere. While the anomaly due to the aeolian source is probably of little practical interest, the anomalies due to the hydrothermal and sediment sources can be seen to underpredict the true contribution by as much as 0.1 nM. The underprediction reaches to the surface in the Southern Ocean, a key iron-limited high-nutrient low-chlorophyll region where the iron budget is of particular interest.

Because dFe is most important in the euphotic zone, Figure 3 focuses on the source contributions and anomalies averaged vertically and zonally over the global euphotic zone (the top 73.4 m of the model). First, note that the three source contributions sum to the total iron concentration (solid black line) to numerical precision, i.e.,  $\sum_{i=1}^3 \chi_i = \chi$ , while the anomalies sum to less than the total (thin dashed black line), i.e.,  $\sum_{i=1}^3 \Delta\chi_i < \chi$ .

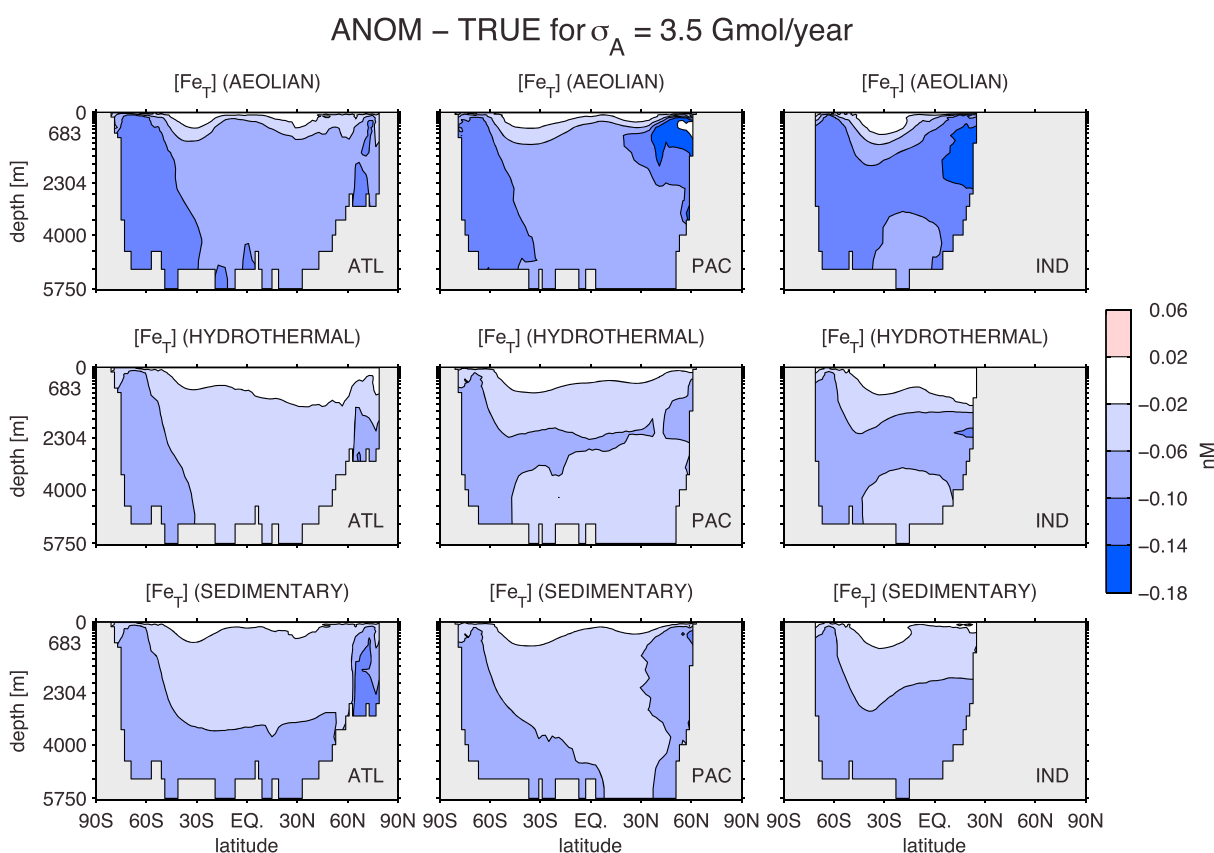


**Figure 2.** The difference between the anomalies due to each source and the true contribution to the dFe concentration from each source.

Roughly 60% of the dFe in the Southern Ocean is of aeolian origin, while the remainder is accounted for by hydrothermal and sedimentary iron in nearly equal measure. While source contributions and anomalies have roughly the same qualitative shape, in the Southern Ocean south of  $\sim 40^\circ\text{S}$  the anomalies underestimate both the hydrothermal and sedimentary contributions by roughly a factor of 2. Specifically, the hydrothermal anomaly is only  $\sim 10\%$  of the total, while the true contribution is  $\sim 20\%$ .

To gain insight into the origin of dFe in the Southern Ocean and to understand better why the nonlinearity of the scavenging, as manifest by the discrepancy between true contributions and anomalies, is largest in the Southern Ocean, we now examine the mean iron age.

### 3.2. Iron Age

#### 3.2.1. Zonally Averaged Mean Iron Age

Figure 4 shows the zonally averaged mean iron ages  $\Gamma_{\text{Fe}}$  of the total dFe due to all sources and separately for the aeolian, sedimentary, and hydrothermal components for our representative case of  $\sigma_A = 3.5$  Gmol/yr. Although the zonal mean aeolian and sedimentary age patterns are roughly similar, the mean iron age of total dFe (Figure 4, first row) is dominated by the aeolian component because the total iron age is the concentration weighted average of the component iron ages (equation (9)) and aeolian iron is the dominant contributor for the family of solutions analyzed. The mean age of aeolian iron (Figure 4, second row) is smallest near the surface where new aeolian iron is constantly being injected and where the scavenging is also strong. Surface-injected dFe that is taken up biologically is “pumped” to depth with sinking organic matter and then released back into the water column as regenerated dFe when the organic matter remineralizes. In the deep ocean, the exported iron is subjected to much weaker scavenging and able to survive for longer. (The scavenging rate constant in the estimates of *Frants et al.* [2016] decreases roughly like the inverse depth squared.) Thus, as long as deep dFe is not brought to surface regions where atmospheric deposition strongly dilutes the old iron molecules with young ones, and/or where biological production and hence scavenging is strong, “killing off” the dFe molecules, the population of dFe molecules can attain a relatively old mean

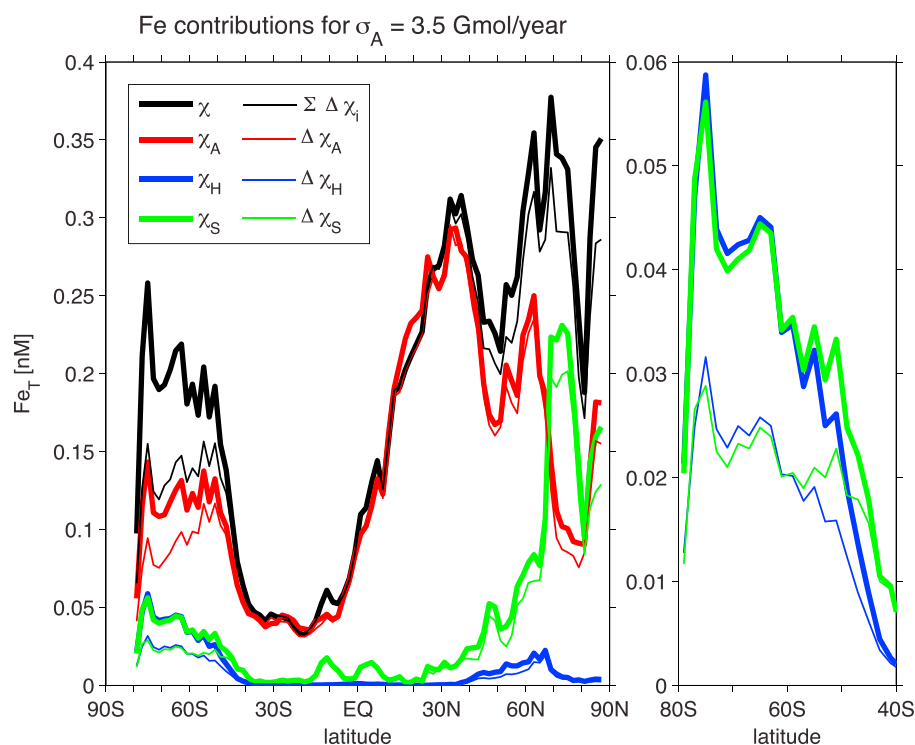


**Figure 3.** (left) Comparison of the euphotic-zone dFe concentrations due to each source,  $\chi_A$  (aeolian),  $\chi_H$  (hydrothermal), and  $\chi_S$  (sedimentary) (thick lines) with the corresponding anomalies  $\Delta\chi_A$ ,  $\Delta\chi_H$ , and  $\Delta\chi_S$  (thin lines) defined as the difference in concentrations with and without the source in question. The  $\chi_i$  and  $\Delta\chi_i$  have been vertically and zonally averaged over the global euphotic zone. (right) The hydrothermal and sedimentary dFe contributions and anomalies plotted on a magnified scale for latitudes 80°S to 40°S.

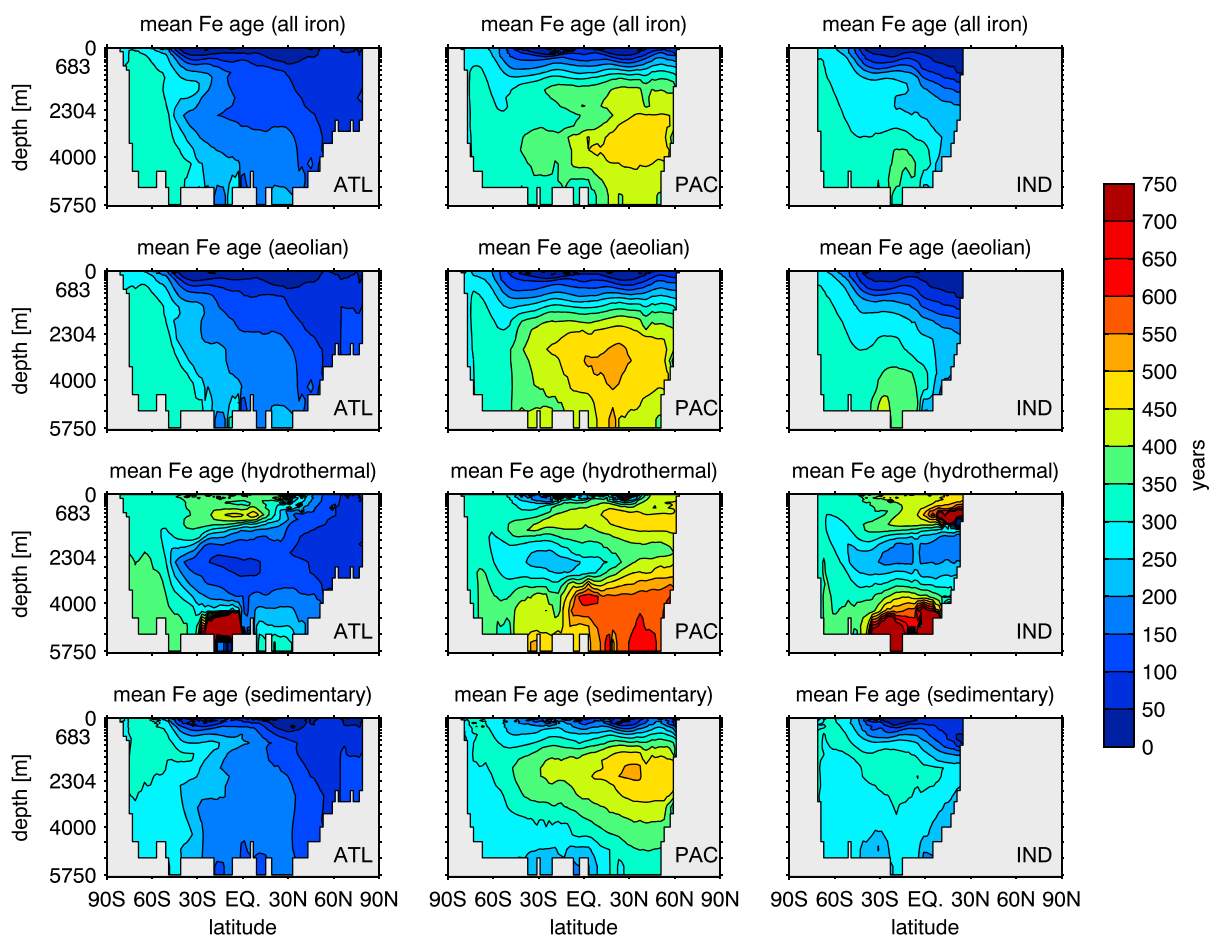
iron age. Consistent with this picture, the oldest aeolian iron is found in the old waters of the deep North Pacific. In the Southern Ocean, particularly in the Pacific sector, a tongue of old iron age is seen to reach toward the surface.

The mean ages of hydrothermal dFe (Figure 4, third row) are smallest around the hydrothermal sources where hydrothermal iron is “born.” The tongues of diluted hydrothermal iron that can be seen upwelling in the Southern Ocean in Figure 1 manifest as tongues of relatively younger mean hydrothermal iron age. The oldest hydrothermal ages are found below the mean injection depths. In these abyssal waters, transport is slow and the scavenging rate is small so that the iron there can attain mean ages in excess of 500 years. Similarly, above the hydrothermal iron plumes, scavenging is still weak and the mean hydrothermal iron can be as old as 400–500 years in a broad layer around ~700 m depth. Near the surface of the Pacific subtropical gyres, the mean iron age is only a few decades. This young surface layer is due to some near-surface hydrothermal sources. The concentration of upwelled old hydrothermal iron is near zero in the subtropical gyres (less than  $10^{-3}$  nM), and the presence of even a small amount of near-surface-injected hydrothermal dFe suffices to push the mean hydrothermal iron age to near zero in these regions. (We verified that zeroing the hydrothermal source above 317 m depth brings the surface age up to more than 250 years throughout the Pacific. In the North Pacific, the small hydrothermal source driving the mean age to near zero lies above 187 m depth.)

The mean age of sedimentary iron (Figure 4, fourth row) is relatively young near the ocean bottom and at the sea surface and relatively old in the old waters of the North Pacific, where sedimentary iron can accumulate for a long time before being scavenged. The elevated ligand concentrations in old waters also reduce conversion to free iron and hence scavenging. In the Southern Ocean, upwelling old sedimentary iron manifests as a tongue of relatively old sedimentary mean iron age.

### 3.2.2. Mean Iron Age in the Euphotic Zone

Figure 5 shows maps of the mean iron age in the euphotic zone computed for the total dFe and separately for each of the three source components, together with corresponding maps of the euphotic-zone dFe concentration. The near-zero euphotic concentrations in the Pacific and South Atlantic subtropical gyres make the

mean Fe age for  $\sigma_A = 3.5$  Gmol/year


**Figure 4.** Mean iron age since injection by the total source (all iron) and the mean iron ages of the aeolian, hydrothermal, and sedimentary source components, zonally averaged for each basin.

calculation of the mean iron age near the surface numerically delicate because of the division by the mean concentration in equation (7). To make the calculation more robust, we assigned to each surface grid box the mean iron age computed using equation (8) for the 18 grid boxes consisting of the surface grid box itself, its eight nearest and next nearest surface neighbors, and the nine grid boxes immediately below. The resulting 18-box average concentration is sufficiently far from zero to allow stable division.

Because the dominant contributor to the dFe concentration in the euphotic zone is aeolian iron, the mean iron age of total dFe is dominantly shaped by the mean aeolian iron age. As already quantified in Figure 3, roughly 40% of the Southern Ocean euphotic dFe is due to hydrothermal and sedimentary iron (roughly 20% due to each). In the Arctic Ocean, sedimentary iron also makes a significant contribution, although we caution that the Arctic circulation used is poorly constrained. While concentrations of hydrothermal and sedimentary iron are relatively low in the euphotic zone, they are characterized by distinct mean iron age patterns.

The euphotic mean iron age of the total dFe (Figure 5, first row) is younger than 30 years in most places but elevated in the eastern tropical Pacific (ETP) and in the subpolar oceans, where old iron upwells and/or is mixed into the euphotic zone from depth. The mean iron age in the ETP and in the subpolar North Atlantic reaches around a hundred years and is a few decades older in the subpolar North Pacific. However, the Southern Ocean really stands out with a circumpolar band of old mean iron ages that reach  $\sim 300$  years near Antarctica. This shows that a significant fraction, to be quantified further below, of the dFe in the Southern Ocean euphotic zone is transported there from depth. The mean aeolian iron ages are very similar to the mean total iron ages

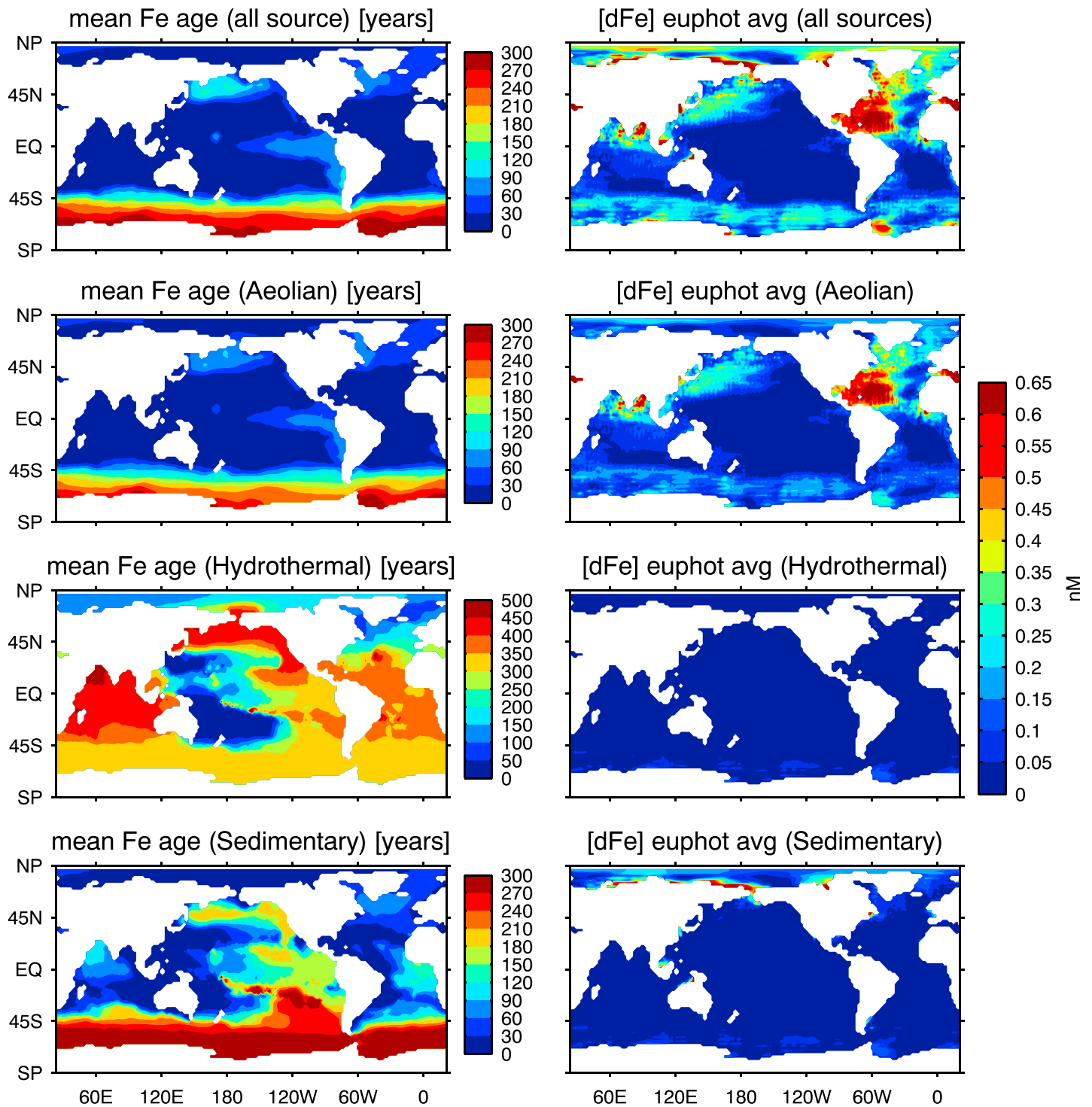


**Figure 5.** (left column) Euphotic-zone averages of the mean iron ages for the total dFe concentration and for the contribution from each source, as indicated. Note that the color scale for hydrothermal mean iron age has a maximum of 500 years, while the other color scales for mean iron age extend to only 300 years. (right column) Corresponding euphotic-zone dFe concentrations. The fields plotted are for the  $\sigma_A = 3.5$  Gmol/yr case.

except that the aeolian dFe is a few decades younger in the subpolar and polar oceans where the sedimentary and hydrothermal sources make nonnegligible contributions (see also Figure 3).

Figure 5 shows that in the euphotic zone sedimentary and aeolian iron have broadly similar mean age patterns, with old sedimentary iron found in regions of upwelling and/or vertical mixing. In the upwelling/mixing regions, the maximum mean sedimentary iron ages are roughly 100 years older than the corresponding mean aeolian iron ages. The mean hydrothermal iron age is 300 years or older across most of the global euphotic zone except for “pockets” such as the Pacific subtropical gyres and the subpolar North Atlantic where some hydrothermal sources are located near the surface, as discussed above. That hydrothermal iron has the oldest surface ages is a consequence of its generally deep sources and the time required to ventilate deep water masses.

### 3.2.3. Iron Age Spectra

The underlying age spectra contain much more detailed transport information than their mean,  $\Gamma_{\text{Fe}}$ . Because aeolian iron dominates the overall mean iron age and couples most directly to the biological pump, we focus in Figure 6 on aeolian iron for locations in the subtropical North Atlantic, subtropical North Pacific, and in the Atlantic and Pacific sectors of the Southern Ocean. As a consequence of the eddy-diffusive component of iron transport, all age spectra are highly skewed with a mean that is longer than the mode (the age where the distribution has its maximum).

At the subtropical Atlantic location of Figure 6, aeolian input is high and correspondingly the near-surface iron population has a very narrow age spectrum with a young mean iron age. With increasing depth, the distribution broadens out, while qualitatively preserving its overall shape (its width actually becomes narrower on the scale of the mean, presumably because the very young peak due to the biological pump attenuates with depth). The mean iron age increases with depth to about 200 years in the abyss as scavenging sharply decreases, and dFe is able to survive for longer. At the location in the subtropical North Pacific the overall behavior is similar, but the mean iron age increases more rapidly with depth, where the shape of the iron-age spectrum changes qualitatively: At middepth the age spectrum is bimodal with a relatively young peak (at a few decades) of new iron biologically pumped to depth and a broad older peak with a long tail characterizing the population of old iron that is surviving in the old waters of the deep Pacific where scavenging is additionally suppressed in our inverse-model estimate by an increased ligand concentration.

The locations in the Southern Ocean show qualitatively different behavior in Figure 6: The aeolian age spectra are broad throughout the water column with mean aeolian iron ages around roughly 300 years that vary little with depth. However, even in the Southern Ocean, where aeolian input is sharply decreased from its low-latitude highs, with only 6.6% of the global total south of 46°S, there is a pronounced young peak in the upper water column. The peak near zero age at 137 m depth is due to direct aeolian deposition near the location examined.

To quantify the effect of transport paths from aeolian sources within the Southern Ocean as well as from relatively fast paths from outside the Southern Ocean via the wind-driven thermocline circulation, Figure 6 also shows (blue lines) the iron-age spectra with these paths excluded for the two locations in the Southern Ocean. Paths were excluded by separately labeling (i) aeolian iron from sources south of 46°S and (ii) aeolian iron from sources elsewhere that never ventured below 1005 m depth and then subtracting the contributions due to (i) and (ii) from the total. For (ii), excursions below 1005 m were excluded by imposing fast relaxation to zero concentration below 1005 m depth. The resulting age spectra, conditional on the iron having originated north of 46°S and having ventured below 1005 m depth, go to zero at zero age with a mode between roughly 100 and 200 years. As the corresponding cumulative distributions show, when integrated over all iron ages, these deep paths from outside the Southern Ocean account for ~70% of the aeolian iron near the surface and ~80% at depth for the locations examined.

To quantify the contributions of deep paths from sources outside the Southern Ocean, as opposed to from all paths within the Southern Ocean, Figure 7 shows the corresponding zonally averaged dFe concentrations. Aeolian iron from sources south of 46°S amounts to as much as ~30% of the total dFe concentration near the surface at 50°S and to ~10% throughout the deep Southern Ocean water column. Aeolian iron from sources north of 46°S via paths that never ventured below 1005 m depth accounts for about 40% of the total dFe near 46°S, which falls to less than ~15% near 60°S. The deep paths from sources north of 46°S (Figure 7, bottom row) contribute as much as 75% of the dFe near the Antarctic coast at the surface (about 85% at depth) and account for the long mean iron ages in the high-latitude euphotic zone.

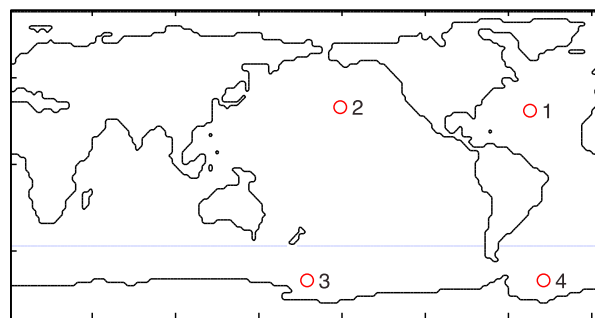
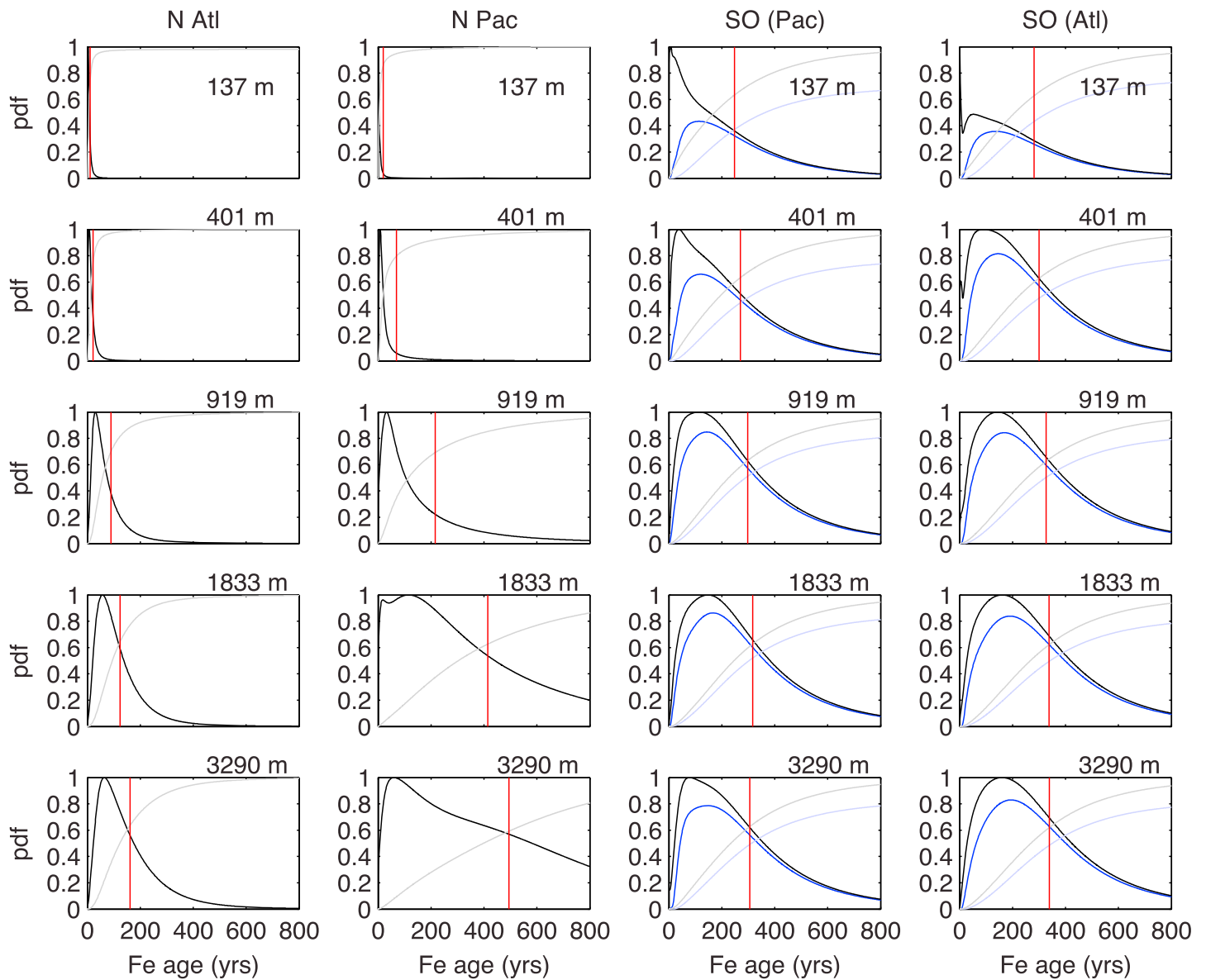


**Figure 6.** Aeolian iron-age spectra at five depths for locations in the North Atlantic (31°N, 47°W), Southern Ocean (Atlantic sector, 67°S, 39°W), Southern Ocean (Pacific sector, 67°S, 179°E), and North Pacific (33°N, 161°W), as indicated for the case of  $\sigma_A = 3.5$  Gmol/yr. The dark black line is the iron-age spectrum regardless of pathway with its maximum value scaled to unity. The dark blue line is the iron-age spectrum of iron that passed at least once below 1005 m depth after injection from sources north of 46°S. The grey and light blue curves are the corresponding cumulative integrals of the iron-age spectra normalized so the age spectra regardless of path (grey) integrate to unity, while the path-conditioned age spectra (blue) integrate to the fraction of aeolian iron that arrived at the point of interest from north of 46°S via deep paths. The red vertical lines indicate the mean aeolian iron age,  $\Gamma_{Fe}$  (regardless of path).

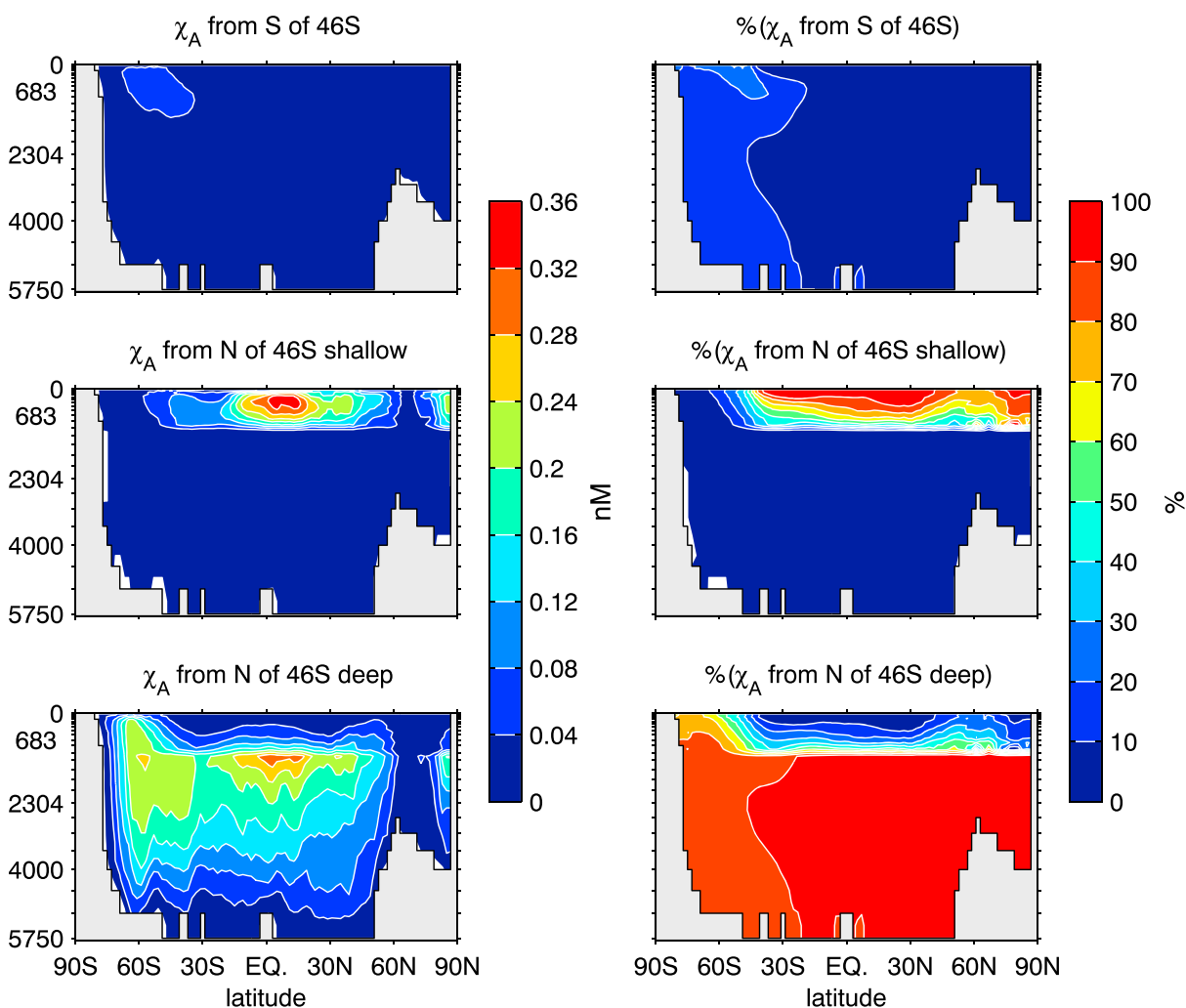


**Figure 7.** (top left) Concentration of aeolian iron due to sources south of 46°S. (middle left) Concentration of aeolian iron due to sources north of 46°S via paths that never ventured below 1005 m depth. (bottom left) The complement of the two panels above, that is, the concentration of aeolian iron due to sources north of 46°S via deep paths that ventured at least once below 1005 m depth. (right column) The same quantities, expressed as a percentage of the total zonally averaged aeolian dFe concentration, so that the three right panels add to unity. The fields plotted are for the  $\sigma_A = 3.5$  Gmol/yr case.

### 3.3. Systematic Variation Across Family of Solutions

So far we have presented results for aeolian source strength  $\sigma_A = 3.5$  Gmol/yr, which is qualitatively representative of our entire family of solutions. However, the true value of  $\sigma_A$  is highly uncertain, with literature estimates ranging from 0.96 to 41 Gmol Fe/yr [Fung et al., 2000; Fan et al., 2006; Tagliabue et al., 2016]. We now examine the quantitative systematic variations of our diagnostics across the family of optimized solutions with  $\sigma_A$  ranging from 0.3 to 14 Gmol/yr. These variations not only directly quantify the sensitivity to  $\sigma_A$  but also to the maximal Fe:P uptake ratio,  $R_0$ , and to the scavenging rate constant,  $k_{sc}$ , which, for this family of solutions, are linearly correlated with  $\sigma_A$ :  $R_0 = [(1.50 \pm 0.06) \times \sigma_A / (\text{Gmol Fe yr}^{-1}) \pm 0.2]$  mmol Fe/mol P, while  $k_{sc} = [(2.9 \pm 0.1) \times \sigma_A / (\text{Gmol Fe yr}^{-1}) - (1.7 \pm 0.4)] \text{ yr}^{-1}$ . We stress that these correlations are not causal but merely reflect the fact that the optimization compensates stronger aeolian input by stronger biological cycling and scavenging to keep the dFe concentrations close to the observations.

When we compute the source contributions and mean iron ages for the small- and large- $\sigma_A$  members of the family of solutions, we find that the qualitative features are similar to the  $\sigma_A = 3.5$  Gmol/yr case. For example, for all family members, the Southern Ocean euphotic zone has the oldest mean iron ages and its dFe

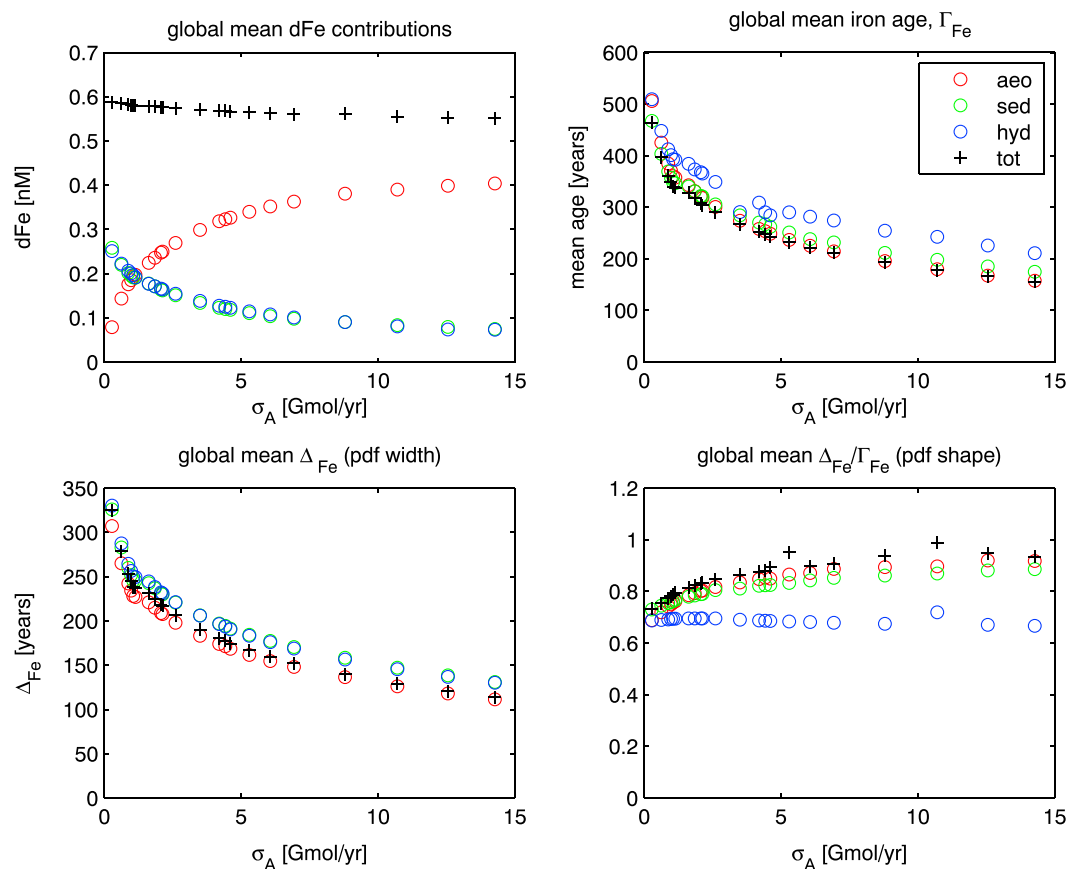


**Figure 8.** The dependence of volume-weighted global mean quantities on the strength  $\sigma_A$  of the aeolian source: (top left) The total iron concentration and the concentrations due to each source. (top right) The mean iron age  $\Gamma_{Fe}$  for the total dFe and for the component due to each source. (bottom left) The corresponding widths  $\Delta_{Fe}$  of the iron-age spectra and (bottom right) the width-to-mean shape parameters  $\Delta_{Fe}/\Gamma_{Fe}$  of the iron-age spectra.

is supplied primarily from sources north of 46°S and reaches the Southern Ocean via deep paths. However, there are quantitative differences. The maximum zonally averaged fraction of aeolian dFe in the Southern Ocean euphotic zone supplied via deep paths from north of 46°S varies from 71% to 83%, and the maximum zonally averaged euphotic-zone mean aeolian iron age ranges from 182 to 335 years as  $\sigma_A$  is decreased from 6.1 to 1.1 Gmol/yr.

While the spatial patterns of the mean iron age and of the source contributions are insensitive to the value of the aeolian source strength  $\sigma_A$ , the value of  $\sigma_A$  does set the amplitudes of these patterns. We therefore summarize in Figure 8 the systematic variations with  $\sigma_A$  in terms of the globally averaged dFe concentrations from each source and their globally averaged mean iron ages  $\Gamma_{Fe}$ , age spectrum widths  $\Delta_{Fe}$ , and the width-to-mean shape parameter  $\Delta_{Fe}/\Gamma_{Fe}$ . The width  $\Delta_{Fe}$  is conventionally defined [e.g., Hall and Plumb, 1994] in terms of the centered second moment of the age spectrum as  $2\Delta_{Fe}^2 \equiv \langle (t - \Gamma_{Fe})^2 g \rangle / \langle g \rangle$ .

Figure 8 shows that the global mean dFe concentration changes little with  $\sigma_A$ , being constrained in our inverse model by the observations. The aeolian dFe component does not increase in proportion to  $\sigma_A$  because as  $\sigma_A$  is increased, the inverse-model optimized scavenging rate must also increase to keep dFe concentrations close to observed values. Nevertheless, the aeolian dFe component does increase, but the hydrothermal and sedimentary components decrease by about the same amount to keep the total global mean dFe concentration approximately constant. This decrease is due to increased scavenging—the globally integrated hydrothermal and sedimentary sources remain roughly constant across the family of solutions [Frants et al., 2016].

Although the global mean iron age is a different quantity than the typically shorter bulk iron residence time (e.g., 1.8 times shorter for  $\sigma_A = 3.5$  Gmol/yr), the two global timescales have broadly similar systematics across our family of estimates. The bulk residence time,  $\tau_T$ , is given by the ratio of the observationally constrained global dFe inventory to the total source strength  $\sigma_T = \sigma_A + \sigma_H + \sigma_S$ , where  $\sigma_H$  and  $\sigma_S$  are the global integrals of  $S_H$  and  $S_S$ . Therefore, as the steady state source-to-sink flow rate  $\sigma_T$  is increased by increasing  $\sigma_A$ , the bulk residence time  $\tau_T$  decreases like  $1/\sigma_T$  [Frants *et al.*, 2016]. For the  $\sigma_A = 3.5$  Gmol/yr case of our inverse model,  $\tau_T = 150$  years, which is comparable to the 42 year residence time of the BLING model with  $\sigma_A = 3.3$  Gmol/yr [Galbraith *et al.*, 2010], considering that the BLING sediment source is an order of magnitude larger than ours. (Because the model of Frants *et al.* [2016] neither parameterizes high-resolution topography nor represents explicit precipitation of high dFe concentrations, we consider the sediment sources of the inverse-model estimates to be the net sediment sources, that is, the sediment sources in excess of high collocated sinks. We return to this point in section 4 below.) Across our family of solutions, as  $\sigma_A$  ranges from 0.3 to 14 Gmol/yr, the bulk residence time ranges from 420 to 45 years, spanning much of the spread in aeolian source strength and bulk residence time among published iron models [e.g., Tagliabue *et al.*, 2016]. We expect the global mean iron age to similarly decrease with increasing  $\sigma_A$  roughly in proportion to  $1/\sigma_T$ . This decrease with  $\sigma_A$  can be seen in Figure 8, and a plot of the global mean  $\Gamma_{Fe}$  versus  $1/\sigma_T$  (not shown) falls roughly on a straight line. The plot of the global mean ratio  $\Delta_{Fe}/\Gamma_{Fe}$  versus  $\sigma_A$  in Figure 8 shows that the decrease in the mean iron age with increasing  $\sigma_A$  is, on a global average, accompanied by a modest broadening of the shape of the iron age spectra: As the global mean  $\Gamma_{Fe}$  decreases across the range of  $\sigma_A$  explored, so does the global mean width  $\Delta_{Fe}$ , but slightly less so, increasing the shape parameters  $\Delta_{Fe}/\Gamma_{Fe}$  of aeolian and sedimentary dFe from roughly 0.7 to 0.9. The shape parameter of the hydrothermal iron-age spectrum changes very little, lying between 0.67 and 0.72 across the entire range of  $\sigma_A$ .

The ratio of the true hydrothermal and sedimentary dFe contributions to the corresponding anomalies is not very sensitive to the value of  $\sigma_A$ . Throughout the family of solutions, the anomalies underestimate the true contributions in the Southern Ocean euphotic zone by a factor of  $\sim 1.5$  to  $\sim 2$  (see Figure B1). For completeness, Figure B2 shows the zonally averaged percent contribution of hydrothermal and sedimentary dFe in the euphotic zone as a function of  $\sigma_A$ , and Figure B3 shows the zonally averaged mean iron age of each source component in the euphotic zone as a function of  $\sigma_A$ . The systematic variations in the euphotic zone mirror those of the globally integrated bulk quantities of Figure 8. Like the global mean contributions, the hydrothermal and sedimentary euphotic-zone contributions become smaller with increasing aeolian source strength,  $\sigma_A$ . In the Southern Ocean the  $\sim 20\%$  hydrothermal and sedimentary contributions for  $\sigma_A = 3.5$  Gmol/yr increase to  $\sim 30\%$  for  $\sigma_A = 1.1$  Gmol/yr and decrease to  $\sim 15\%$  for  $\sigma_A = 6.1$  Gmol/yr. (For  $\sigma_A > 6.1$  Gmol/yr, the surface dFe field displays unrealistic features [Frants *et al.*, 2016].) Similarly, the maximum zonally averaged aeolian mean iron age in the Southern Ocean euphotic zone of  $\sim 260$  years for  $\sigma_A = 3.5$  Gmol/yr increases to  $\sim 360$  years for  $\sigma_A = 1.1$  Gmol/yr and decreases to  $\sim 210$  years for  $\sigma_A = 6.1$  Gmol/yr.

#### 4. Model Caveats and Discussion

We analyzed the transport of dissolved iron for the family of inverse-model estimates of the marine iron cycle by Frants *et al.* [2016]. Our analysis is rigorous within the context of these estimates and illustrates the utility of the source-contribution and iron-age diagnostics. However, our conclusions are of course only as robust as the estimates of the iron cycle. It is therefore important to keep in mind several caveats. Although the data-assimilated circulation accurately captures the transport of key steady and transient tracers and can hence be considered to be a ventilation-weighted annual mean, it is still steady and any seasonal or interannual effects cannot be captured. Small-scale iron sources from island shelves, glaciers, and episodic dust events also cannot be captured by our steady state, coarse-resolution analysis.

Other caveats concern the model of the iron cycle itself. In the model of Frants *et al.* [2016] biological production is prescribed from a phosphate cycling model that has been optimized against the World Ocean Atlas climatology [Garcia *et al.*, 2010]. While this implicitly accounts for the effects of light and iron limitation on biological production, the source anomalies considered here are not influenced by nonlinear feedbacks of dFe changes on production. The difference between source anomalies and source contributions considered

here is therefore only due to the nonlinear scavenging. If the iron and phosphate cycle were coupled, the source anomalies would likely be different. However, the source contributions within the unperturbed iron cycle, computed precisely here from linear labeling tracers, would be unchanged given identical phosphate uptake. While it is possible that the anomalies due to the feedback on production counter those due to scavenging, it is equally likely that the discrepancy between contributions and source anomalies would be larger still for the coupled system. We emphasize that our diagnostics for iron source attribution and iron age do not require that biological uptake be prescribed—these diagnostics can be applied equally well to a model with fully interactive biological nutrient utilization.

The model of *Frants et al.* [2016] does not allow scavenged iron to redissolve. If some or all scavenged iron could redissolve before ultimately being lost, with all other parameters unchanged, the global mean iron age would increase because iron is allowed to “live” longer. However, without reoptimizing parameters, such a model would produce unrealistic dFe fields. To explore the effect of redissolution on our results, we replaced the scavenging rate  $J_{sc}$  in equation (1) with  $(1 - \lambda S_{sc})J_{sc}$ , where  $S_{sc}$  is an operator that instantly reassigns the scavenging rate per unit volume in every model layer to a source of redissolved iron distributed in the water column below, and  $\lambda$  is the fraction of scavenged iron that is recyclable in this way. The flux of scavenged iron into the seafloor is assumed to be permanently lost for simplicity. The transport and dissolution of scavenged iron is accomplished with the divergence of a power law particle flux profile with the same power used in the organic matter sinking and remineralization operator  $S$ . For the extreme case of  $\lambda = 1$  and all other parameters unchanged, the global mean iron age increases by  $\sim 20\%$ , but the dFe concentrations are nearly a factor of 2 too high. When the scavenging parameters are reoptimized, the root-mean-square (RMS) mismatch with observations is within 1% of its value without dissolution. The optimized value of  $\lambda$  is  $\sim 0.5$  or less, depending on the aeolian source strength.

For the reoptimized iron cycling with redissolution, the dFe fields and the diagnostics considered here turn out to change very little. By taking the difference between optimized solutions with and without redissolution, the following changes can be quantified. The global mean iron age decreases by  $\sim 4\%$ . The local zonal-mean iron age of all source components decreases most places by 5–15%, more at the surface, less at depth. The total dFe concentration decreases by up to 20% near the tropical surface and increases by  $\sim 10\%$  near the bottom, with  $\sim 5\%$  changes most places in the zonal mean. The aeolian dFe contribution increases below the thermocline, with a maximum increase of  $\sim 15\text{--}30\%$  in the middepth northern Pacific and Indian Oceans. The hydrothermal and sedimentary contributions decrease most places by 10–20%, with the largest decreases at the tropical surface and increases near the bottom. The age spectra change only slightly and retain all qualitative features. The Southern Ocean contributions from upwelled iron, the difference between source anomalies and contributions, and the systematic variations of our diagnostics across the family of solutions remain nearly unchanged, with no qualitative changes to our conclusions.

The reason for the robustness of our results to these changes in the scavenging parameterization is as follows: The particle transport and remineralization of the biological pump in the solutions of *Frants et al.* [2016] accomplishes iron transport very similar to that of the combined action of the biological pump and the sinking and redissolving of scavenged iron. Although the biological pump only removes dFe in the top 74 m in our model, the scavenging is also strongest in the upper few hundred meters of the ocean. As far as the dFe distribution is concerned, the interior source of dFe from the redissolution of scavenged iron can be reasonably well approximated by an overactive biological pump. It does mean, however, that  $R_0$  in the family of solutions of *Frants et al.* [2016] must be interpreted not as just the Fe:P ratio of biological uptake but rather as an effective strength of the combined biological and scavenging pump to depth. (Compared to the solutions of *Frants et al.* [2016], the reoptimized states with redissolution no longer vary strongly with aeolian source strength,  $\sigma_A$ , for  $\sigma_A \gtrsim 4$  Gmol/yr.)

Ligands are critically important for determining the amount of scavengable free iron, and one may ask how our assumption of increased ligands in old water influences our results. This ligand enhancement was inspired by *Misumi et al.* [2013], who model their weak-binding (L2) ligand concentrations as a linear function of apparent

oxygen utilization based on the observations of *Yamashita and Tanoue* [2008]. *Kondo et al.* [2012] measured ligand concentrations of  $\sim 2$  nM in the deep North Pacific at  $160^\circ$ W, although such high ligands were not seen  $\sim 35^\circ$  farther west, consistent with earlier measurements [*Kuma et al.*, 1998; *Nakabayashi et al.*, 2001; *Kuma*, 2003]. Recent modeling by *Völker and Tagliabue* [2015] assumes ligands to degrade with a lifetime that decays exponentially with ligand concentration, leading to ligands that diminish along the deep conveyor circulation. While there are supporting observations in the Atlantic, the model of *Völker and Tagliabue* [2015] does not capture the deep North Pacific ligand data of *Kondo et al.* [2012]. Given the uncertainty in the spatial variability of ligands, we recomputed our diagnostics for the case of zero ligand enhancement in older waters, with the other parameters reoptimized. The effect is a worse fit to the observations, with a dFe field reduced by up to 30% in the middepth North Pacific and increased by up to  $\sim 20\%$  in the deep Atlantic. In the Southern Ocean, the aeolian contribution is decreased by up to 10% near the surface, with corresponding increases in the hydrothermal and sedimentary components, with near zero total change near the surface. The effect on mean age is more modest, with roughly 10% reductions in the North Pacific, 10% increases in the South Pacific, and 10–20% increases in the Atlantic (greater at depth). We consider these changes to be rough estimates of the uncertainty in our diagnostics due to uncertainty in the ligands.

The aeolian sources of the family of solutions examined spans most previously published values for these sources, with only three of the 12 models of the intercomparison of *Tagliabue et al.* [2016] exceeding 14 Gmol/yr by at most a factor of  $\sim 2$ , with mean and median source strengths being 12. and 3.5 Gmol/yr, respectively. *Luo et al.* [2008] estimate the aeolian source of dFe to the ocean to be  $\sim 6$  Gmol/yr. Our hydrothermal source of  $\sim 0.6$ – $0.7$  Gmol/yr is similar to the observational estimate of *Fitzsimmons et al.* [2014]. *Tagliabue et al.* [2010] used the NEMO-PISCES model with a hydrothermal source of similar magnitude, but since then the hydrothermal sources of the PISCES models have been increased to 11 Gmol/yr to fit new GEOTRACES data in the Pacific [*Resing et al.*, 2015]. The current BEC model also has a larger hydrothermal source of 18 Gmol/yr [*Moore et al.*, 2013; *Tagliabue et al.*, 2016]. Possibly these models need higher hydrothermal sources because they also need more aggressive scavenging to balance large sediment sources. On the other hand, data from the recent Pacific GEOTRACES sections were not yet available when the model of *Frants et al.* [2016] was optimized, and it is entirely possible that including these data would lead to an increase in the inferred hydrothermal sources.

The sediment source of the family of solutions of *Frants et al.* [2016] should not be thought of as the gross dFe source from sediments but as the *net* source in excess of local strong sinks. Large gross sediment sources do not allow the inverse model to match observed dFe concentrations because key sinks that moderate the dFe concentration by balancing such high sources are either not triggered at coarse resolution or absent from our model. Specifically, we do not parameterize subgrid topography and hence underestimate sediment sources on the shelves and near islands. The absence of shallow subgrid sedimentary sources also means the absence of large scavenging rates in shallow waters where the organic particle concentration is highest. Thus, not resolving subgrid topography means that we miss both high sources and corresponding nearly colocated high sinks of sedimentary iron. Furthermore, we do not enhance scavenging rate coefficients for high dFe concentration, which is another mechanism for controlling dFe concentrations in the presence of high sediment sources. *Dale et al.* [2015] estimate the gross source from continental margin sediments to be  $109 \pm 55$  Gmol/yr. However, such high sources are likely largely balanced by local sinks (*Dale et al.* [2015] also make this point), and the net sediment source relevant for determining the dFe concentration away from the coasts is likely much smaller. This reasoning is supported by the fact that with only sediment sources (zero aeolian and hydrothermal sources and no changes to the other parameters), our model produces Southern Ocean dFe concentrations of  $\sim 0.1$  nM in the upper 100 m and around 0.22 nM at depth (for both optimized scavenging parameterizations considered). This is comparable in magnitude to *Moore and Braucher's* [2008] sediment-only runs with a source that is 2 orders of magnitude larger than ours, although our model only barely captures plumes in the middepth thermocline downstream from shelf sources such as New Zealand and Patagonia. We therefore consider the sediment source of our family of solutions to be the net source in excess of local strong sinks. Locally high concentrations and sedimentary dFe contributions near the shelves are not captured. Our zonal average contributions are thus likely an underestimate, but because

the shelves and associated plumes do not occupy a large fractional volume, we expect our zonally averaged sediment contributions to have qualitatively reasonable open ocean patterns (i.e., away from land in the zonal average).

In the context of an inverse model, it is perhaps also worth remarking that the complexity of the model should be commensurate with the detail constrainable from the available observations. Even with the GEOTRACES intermediate data product, which does not include Pacific transects, the available iron observations are still sparse and the iron cycle is not nearly as well constrained as the macronutrient cycles for which gridded climatological nutrient concentrations are available. Specifically, the estimates of *Frants et al.* [2016] typically have an RMS dFe concentration mismatch of 0.19 nM globally (0.21 nM in the Pacific and 0.14 nM in the Atlantic). While this is substantial, it compares favorably with more complex models [e.g., *Moore and Braucher*, 2008; *Misumi et al.*, 2011], which have similar or even larger misfits [*Frants et al.*, 2016].

Despite these caveats, the estimates of the iron cycle employed here produce dFe concentrations that match the basin-scale observed vertical profiles to within their observational uncertainties [*Frants et al.*, 2016, Figure 3], and the qualitative aspects of our findings here are robust across a wide family of solutions, all members of which are about equally consistent with the available observations.

## 5. Conclusions

We have introduced diagnostics that partition dFe according to source and according to its age since injection by the source. The general utility of these diagnostics and the concept of iron-age spectra and mean iron age, which can be applied to any model of the marine iron cycle, was illustrated for the family of data-constrained solutions by *Frants et al.* [2016]. While this family is based on a highly simplified model of the iron cycle, our findings are qualitatively robust to changes in the scavenging parameterization. The sensitivity to assumed ligand enhancement in old waters and the systematic variations over an order of magnitude range of the aeolian source strength provide a measure of the uncertainty.

We have shown that assessing the importance of the hydrothermal or sedimentary source to the dFe concentration in terms of the anomaly with the source removed underestimates the true contributions by these sources within the unperturbed iron cycle. This is because the iron cycle is nonlinear and operates differently with and without the source in question. The nonlinearities at play for the iron model analyzed are due only to the nonlinear scavenging. Because biological production is prescribed, the nonlinear feedbacks of altered dFe concentrations on production are not captured by the anomalies considered. The effect of the scavenging nonlinearity is particularly strong in the Southern Ocean, where the source contributions in the euphotic zone are roughly twice as large as the anomalies.

We stress that the source-attribution diagnostic presented here is useful for analyzing how the iron cycle operates within the unperturbed system for a given set of sources. By contrast, source anomalies quantify the response of the nutrient and carbon cycles to changes in the sources. Whether a source anomaly or source attribution within the unperturbed system is the diagnostic of choice depends on the particular scientific question of interest.

The population of dissolved iron molecules attains a finite mean age because scavenging provides the necessary “death” process. Unlike the ideal mean age of water, the mean iron age need not be zero at the surface and attains large values in the euphotic zone where old regenerated iron that has been shielded from strong scavenging at depth upwells or is mixed to the surface. The mean iron age in the euphotic zone is oldest in the Southern Ocean, where it exceeds several hundred years near Antarctica. The effects of the nonlinearity in the iron scavenging have therefore accumulated over longer times in the Southern Ocean than elsewhere in the euphotic zone, consistent with the large discrepancies between source contributions and source anomalies at high southern latitudes.

The mean iron age is dominated by the aeolian component, which makes the largest contribution to the dFe concentration for the family of estimates analyzed. For an aeolian source strength of 3.5 Gmol/yr, the mean aeolian iron age reaches up to ~300 years in the Southern Ocean, where about 70–80% of the iron is supplied from outside of the Southern Ocean (46°S) via paths that reach below 1005 m depth. Hydrothermal iron in the

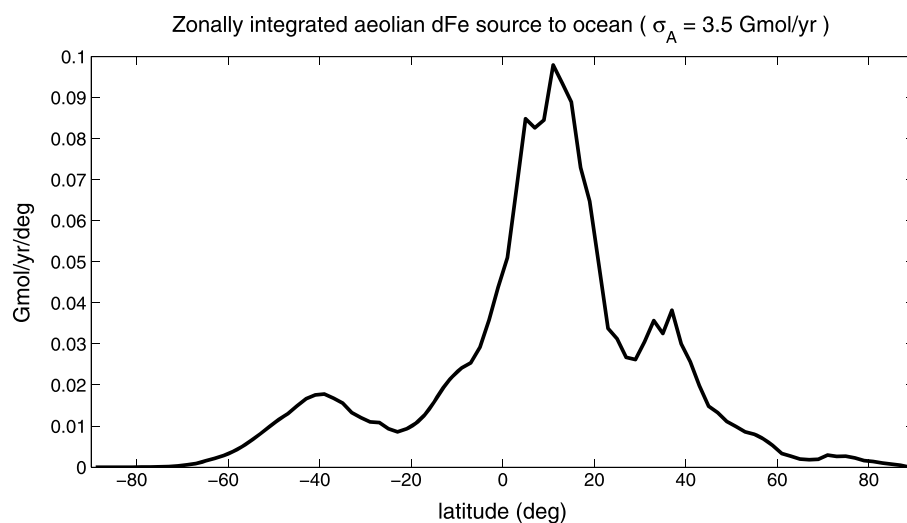


**Figure A1.** The aeolian source of dissolved iron for the oceans, zonally integrated, as a function of latitude. This source has the same shape across our family of solutions. It is plotted to scale here for the case where the global aeolian source to the ocean is  $\sigma_A = 3.5$  Gmol/yr.

euphotic zone has a mean age of hundreds of years, which is a typical timescale for ventilating the middepth ocean where most hydrothermal iron is injected at the mid-ocean ridges.

The results displayed here are qualitatively robust across a family of solutions with widely varying aeolian input ( $\sim 0.3$ – $14$  Gmol/yr), all of which match the observed dFe concentrations to approximately the same degree [Frants *et al.*, 2016]. The spatial patterns of the iron age are similar for all family members, but the amplitude of the iron age decreases with increasing aeolian source strength because the source-to-sink iron cycling rate has to increase to maintain iron inventories constrained by the observations in our inverse model. The factor by which the source anomalies underestimate the true contributions to the dFe concentration from each source depends only weakly on the aeolian source strength and ranges from  $\sim 1.5$  to  $\sim 2$  in the Southern Ocean euphotic zone.

As additional dFe and ligand measurements become available from GEOTRACES and other field campaigns, the considerable uncertainties about the iron cycle will become smaller, and mechanistic models of the iron cycle will become more sophisticated, for example, by including ligands of various lifetimes as explicit tracers. The diagnostic methods presented here for partitioning dFe concentrations into the contributions from different sources and the concept of mean iron age and iron-age spectra should continue to prove useful for understanding how the iron cycle operates. We also hope that the analysis of the iron cycle presented here will provide a useful point of reference for future estimates of the marine iron cycle.

### Appendix A: Aeolian Iron Input

Figure A1 shows the source of aeolian dFe, zonally integrated over the world oceans (land has been excluded) for the case where the globally integrated aeolian source is  $\sigma_A = 3.5$  Gmol/yr. A map of this source is provided by Frants *et al.* [2016]. For other values of the aeolian source strength, the same spatial pattern was used, with an amplitude scaled by  $\sigma_A$ .

### Appendix B: Euphotic-Zone dFe Metrics as a Function of $\sigma_A$

Figure B1 shows that the hydrothermal and sedimentary source anomalies consistently underestimate the true contribution to dFe in the Southern Ocean euphotic zone across our entire family of solutions. The true contributions to the dFe concentrations in the euphotic zone averaged over the Southern Ocean south of  $46^\circ$ S are  $\sim 1.5$  to  $\sim 2$  times larger than the corresponding difference between the solutions with and without the source in question.

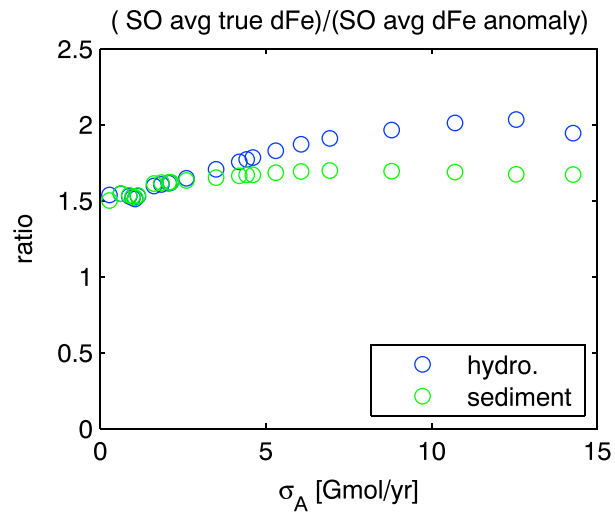


**Figure B1.** The amount by which source anomalies underestimate the true source contributions to dFe in the Southern Ocean (SO) as a function of aeolian source strength  $\sigma_A$ . Plotted are the ratio of the dFe concentration from the source indicated (hydrothermal or sedimentary) to the dFe concentration anomaly if the source in question is removed. The concentrations were averaged over the euphotic zone of the Southern Ocean south of 46°S.

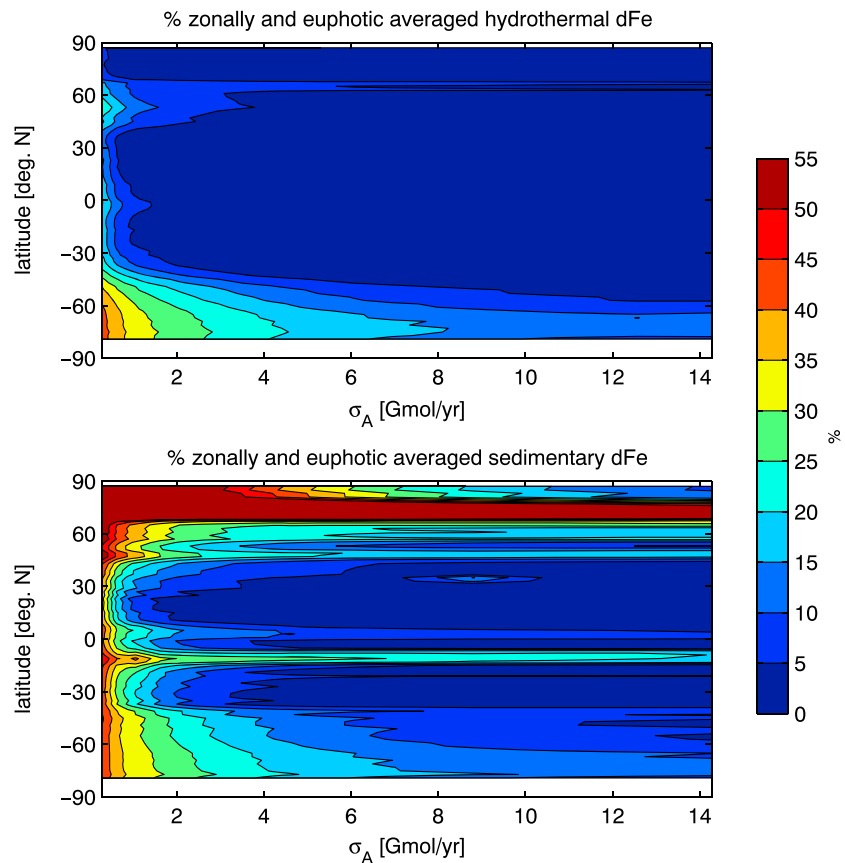


**Figure B2.** The systematic dependence of the percentage of hydrothermal and sedimentary dFe in the euphotic zone on the aeolian source strength  $\sigma_A$ . The percentage is defined in terms of dFe concentrations zonally and vertically averaged over the euphotic zone.

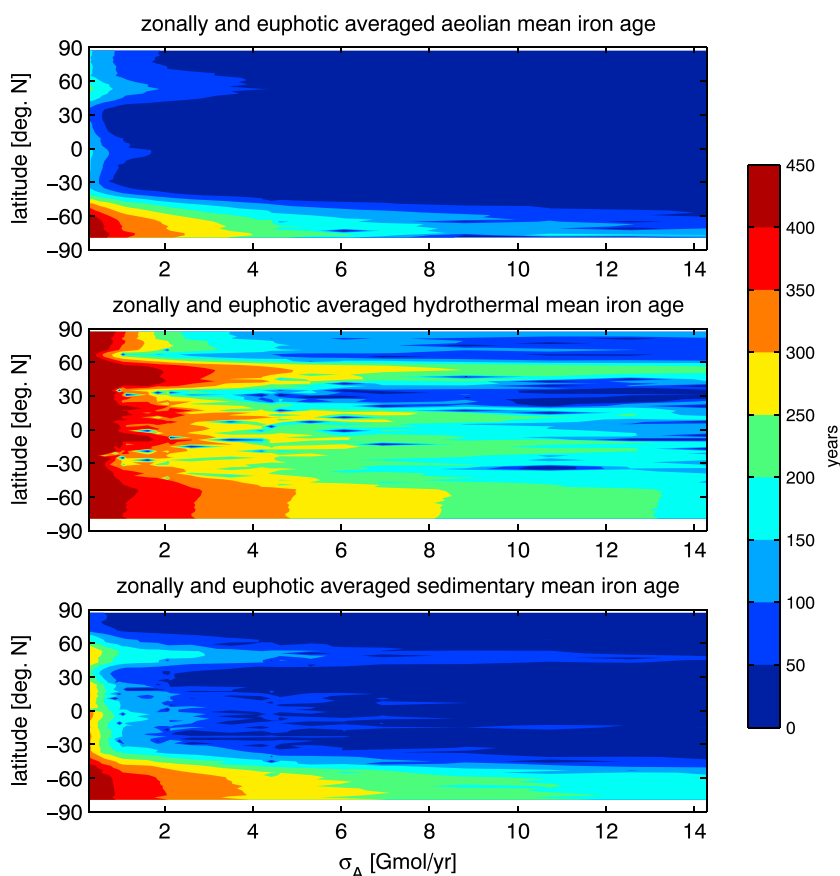


**Figure B3.** The systematic dependence of the mean iron age for each source component of dFe zonally and vertically averaged over the euphotic zone as a function of the aeolian source strength  $\sigma_A$ .

To demonstrate that the systematic dependence on  $\sigma_A$  of the euphotic-zone dFe concentrations and euphotic-zone mean iron ages follows the systematic variations of the global means shown in Figure 8, Figure B2 plots the zonally averaged hydrothermal and sedimentary euphotic-zone dFe concentrations as a function of  $\sigma_A$ , and Figure B3 shows the zonally averaged euphotic-zone mean iron age of each source component as a function of  $\sigma_A$ .

#### Acknowledgments

This work was supported by grant DP120100674 from the Australian Research Council (MH). B.P. gratefully acknowledges scholarship support from the Government of Monaco, the Scientific Centre of Monaco, the Frères Louis et Max Principale Foundation, and the Cuomo Foundation. We thank two anonymous reviewers and A. Tagliabue for their comments that helped to improve the manuscript. All iron data used in this study are available from GEOTRACES (<http://www.bodc.ac.uk/geotraces/data>).

#### References

- Bennett, S. A., E. P. Achterberg, D. P. Connelly, P. J. Statham, G. R. Fones, and C. R. German (2008), The distribution and stabilisation of dissolved Fe in deep-sea hydrothermal plumes, *Earth Planet. Sci. Lett.*, *270*, 157–167.
- Boyd, P. W., et al. (2007), Mesoscale iron enrichment experiments 1993–2005: Synthesis and future directions, *Science*, *315*, 612–617.
- Dale, A. W., L. Nickelsen, F. Scholz, C. Hensen, A. Oschlies, and K. Wallmann (2015), A revised global estimate of dissolved iron fluxes from marine sediments, *Global Biogeochem. Cycles*, *29*, 691–707, doi:10.1002/2014GB005017.
- de Baar, H. J. W., J. T. M. de Jong, D. C. E. Bakker, B. M. Loscher, C. Veth, U. Bathmann, and V. Smetacek (1995), Importance of iron for plankton blooms and carbon dioxide drawdown in the Southern Ocean, *Nature*, *373*, 412–415.
- Dutay, J., et al. (2004), Evaluation of OCMIP-2 ocean models' deep circulation with mantle helium-3, *J. Mar. Syst.*, *48*, 15–36.
- Elrod, V. A., W. M. Berelson, K. H. Coale, and K. S. Johnson (2004), The flux of iron from continental shelf sediments: A missing source of global budgets, *Geophys. Res. Lett.*, *31*, L12307, doi:10.1029/2004GL020216.
- Fan, S. M., W. J. Moxim, and H. Levy II (2006), Aeolian input of bioavailable iron to the ocean, *Geophys. Res. Lett.*, *33*, L07602, doi:10.1029/2005GL024852.
- Fitzsimmons, J. N., E. A. Boyle, and W. J. Jenkins (2014), Distal transport of dissolved hydrothermal iron in the deep South Pacific Ocean, *Proc. Natl. Acad. Sci. U.S.A.*, *111*, 16,654–16,661.
- Frants, M., M. Holzer, T. DeVries, and R. Matear (2016), Constraints on the global marine iron cycle from a simple inverse model, *J. Geophys. Res. Biogeosci.*, *121*, 28–51, doi:10.1002/2015JG003111.
- Fung, I. Y., S. K. Meyn, I. Tegen, S. C. Doney, J. G. John, and J. K. B. Bishop (2000), Iron supply and demand in the upper ocean, *Global Biogeochem. Cycles*, *14*, 281–295.
- Galbraith, E. D., A. Ganadesikan, J. P. Dunne, and M. R. Hiscock (2010), Regional impacts of iron light colimitation in a global biogeochemical model, *Biogeosciences*, *7*, 1043–1064.
- Garcia, H. E., R. A. Locarnini, T. P. Boyer, and J. I. Antonov (2010), World Ocean Atlas 2009, in *Volume 4: Nutrients (Phosphate, Nitrate, Silicate)*, edited by S. Levitus, 398 pp., U.S. Gov. Print. Off., Washington, D. C.

- Hall, T. M., and R. A. Plumb (1994), Age as a diagnostic of stratospheric transport, *J. Geophys. Res.*, *99*, 1259–1070.
- Hansell, D. A., C. A. Carlson, and R. Schlitzer (2012), Net removal of major marine dissolved organic carbon fractions in the subsurface ocean, *Global Biogeochem. Cycles*, *26*, GB1016, doi:10.1029/2011GB004069.
- Hawkes, J. A., J. P. Connelly, M. Gledhill, and E. P. Achterberg (2013), The stabilisation and transportation of dissolved iron from high temperature hydrothermal vent systems, *Earth Planet. Sci. Lett.*, *375*, 280–290.
- Holzer, M., and T. M. Hall (2000), Transit-time and tracer-age distributions in geophysical flows, *J. Atmos. Sci.*, *57*, 3539–3558.
- Holzer, M., and F. W. Primeau (2013), Global teleconnections in the oceanic phosphorus cycle: Patterns, paths and timescales, *J. Geophys. Res. Oceans*, *118*, 1775–1796, doi:10.1002/jgrc.20072.
- Kondo, Y., S. Takeda, and K. Furuya (2012), Distinct trends in dissolved Fe speciation between shallow and deep waters in the Pacific Ocean, *Mar. Chem.*, *134–135*, 18–28, doi:10.1016/j.marchem.2012.03.002.
- Kuma, K. (2003), Control on dissolved iron concentrations in deep waters in the western North Pacific: Iron(III) hydroxide solubility, *J. Geophys. Res.*, *108*(C9), 3289, doi:10.1029/2002JC001481.
- Kuma, K., A. Katsumoto, H. Kawakami, F. Takatori, and K. Matsunaga (1998), Spatial variability of Fe(III) hydroxide solubility in the water column of the northern North Pacific Ocean, *Deep Sea Res., Part I*, *45*, 91–113.
- Landry, M. R., et al. (1997), Iron and grazing constraints on primary production in the central equatorial Pacific: An EqPac synthesis, *Limnol. Oceanogr.*, *42*, 405–418.
- Luo, C., N. Mahowald, T. Bond, P. Chuang, and P. Artaxo (2008), Combustion iron distribution and deposition, *Global Biogeochem. Cycles*, *22*, GB1012, doi:10.1029/2007GB002964.
- Martin, J., R. Gordon, and S. Fitzwater (1990), Iron in Antarctic waters, *Nature*, *345*, 156–158.
- Mawji, E., et al. (2015), The GEOTRACES intermediate data product 2014, *Mar. Chem.*, *177*, 1–8, doi:10.1016/j.marchem.2015.04.005.
- Misumi, K., et al. (2011), Mechanisms controlling dissolved iron distribution in the North Pacific: A model study, *J. Geophys. Res.*, *116*, G03005, doi:10.1029/2010JG001541.
- Misumi, K., K. Lindsay, J. K. Moore, S. C. Doney, D. Tsumune, and Y. Yoshida (2013), Humic substances may control dissolved iron distributions in the global ocean: Implications from numerical simulations, *Global Biogeochem. Cycles*, *27*, 450–462, doi:10.1002/gbc.20039.
- Moore, J. K., and O. Braucher (2008), Sedimentary and mineral dust sources of dissolved iron to the world ocean, *Biogeosciences*, *5*, 631–656.
- Moore, J. K., K. Lindsay, S. C. Doney, M. C. Long, and K. Misumi (2013), Marine ecosystem dynamics and biogeochemical cycling in the Community Earth System Model [CESM1(BGC)]: Comparison of the 1990s with the 2090s under the RCP4.5 and RCP8.5 scenarios, *J. Clim.*, *26*, 9291–9312, doi:10.1175/jcli-d-12-00566.1.
- Nakabayashi, S., M. Kusakabe, K. Kuma, and I. Kudo (2001), Vertical distributions of iron(III), hydroxide solubility, and dissolved iron in the Northwestern North Pacific Ocean, *Geophys. Res. Lett.*, *28*, 4611–4614.
- Primeau, F. W., M. Holzer, and T. DeVries (2013), Southern Ocean nutrient trapping and the efficiency of the biological pump, *J. Geophys. Res. Oceans*, *118*, 2547–2564, doi:10.1002/jgrc.20181.
- Resing, J. A., P. N. Sedwick, C. R. German, W. J. Jenkins, J. W. Moffett, B. M. Sohst, and A. Tagliabue (2015), Basin-scale transport of hydrothermal dissolved metals across the South Pacific Ocean, *Nature*, *523*, 200–203, doi:10.1038/nature14577.
- Sander, S. G., and A. Koschinsky (2011), Metal flux from hydrothermal vents increased by organic complexation, *Nat. Geosci.*, *4*, 145–150, doi:10.1038/NGEO1088.
- Tagliabue, A., et al. (2010), Hydrothermal contribution to the oceanic dissolved iron inventory, *Nat. Geosci.*, *3*, 252–256, doi:10.1038/NGEO818.
- Tagliabue, A., T. Mtshali, O. Aumont, A. R. Bowie, M. B. Klunder, A. N. Roychoudhury, and S. Swart (2012), A global compilation of dissolved iron measurements: Focus on distributions and processes in the Southern Ocean, *Biogeosciences*, *407*, 727–729.
- Tagliabue, A., R. G. Williams, N. Rogan, E. P. Achterberg, and P. W. Boyd (2014), A ventilation-based framework to explain the regeneration-scavenging balance of iron in the ocean, *Geophys. Res. Lett.*, *41*, 7227–7236, doi:10.1002/2014GL061066.
- Tagliabue, A., et al. (2016), How well do global ocean biogeochemistry models simulate dissolved iron distributions?, *Global Biogeochem. Cycles*, *30*, 149–174, doi:10.1002/2015GB005289.
- Teng, Y., F. W. Primeau, J. K. Moore, M. W. Lomas, and A. Martiny (2014), Global-scale variations of the ratios of carbon to phosphorus in exported marine organic matter, *Nat. Geosci.*, *7*, 895–898, doi:10.1038/NGEO2303.
- Völker, C., and A. Tagliabue (2015), Modeling organic iron-binding ligands in a three-dimensional biogeochemical ocean model, *Mar. Chem.*, *173*, 67–77, doi:10.1016/j.marchem.2014.11.008.
- Yamashita, Y., and E. Tanoue (2008), Production of bio-refractory fluorescent dissolved organic matter in the ocean interior, *Nat. Geosci.*, *1*, 579–582, doi:10.1038/ngeo279.

## Erratum

In the originally published version of this article, the address for the University of New South Wales School of Mathematics and Statistics was incorrect. The address has since been corrected, and this version may be considered the authoritative version of record.